Microbeam Production Using Compound Refractive Lenses: Beam Characterization and Applications

Christian G. Schroer[a], Bruno Lengeler[a], Boris Benner[a], Til Florian Günzler[a], Marion Kuhlmann[a], Alexandre S. Simionovici[b], Sylvain Bohic[b], Michael Drakopoulos[b], Anatoly Snigirev[b], Irina Snigireva[b], Walter H. Schröder[c]

[a]II. Physikalisches Institut, Aachen University of Technology RWTH, D-52056 Aachen, Germany
[b]European Synchrotron Radiation Facility (ESRF), B.P. 220, F-39043 Grenoble CEDEX, France
[c]IBI, Forschungszentrum Jülich, D-52425 Jülich, Germany

ABSTRACT

Parabolic compound refractive lenses (PCRLs) are high quality hard x-ray imaging optics that can be used to image a synchrotron source onto a sample in a strongly demagnifying setup. This allows to produce an intensive microbeam with lateral extensions in the (sub-)micrometer range. Aluminium PCRLs can be operated in an energy range from about 10keV to 60keV and withstand the high heat load of the white beam of an ESRF undulator source. The microbeam properties using monochromatic and single undulator harmonic ("pink") radiation are discussed, focusing on beam size, depth of field, background, flux, and gain. The large depth of focus allows to scan fairly large samples (a few millimeters in thickness) with a beam of constant lateral extension. This makes tomographic scanning techniques, such as fluorescence microtomography possible. As applications, fluorescence microtomography of plant samples with sub-cellular resolution and the mapping of trace elements in single cancer cells is shown.

Keywords: x-ray micro beam, compound refractive lenses, scanning microscopy

1. INTRODUCTION

Scanning microscopy with hard x-rays at the synchrotron combines high spatial resolution with x-ray analytical techniques, such as fluorescence, diffraction, small angle scattering, and absorption spectroscopy (XANES, EXAFS). Over the years, a variety of hard x-ray optics have been developed that can be used to produce microbeams, such curved total reflexion mirrors[1,2] and multilayers,[3,4] capillaries,[5,6] diffracting optics, such as Fresnel zone-plates[7] and Bragg-Fresnel optics,[8] and refractive optics,[9–13] such as compound refractive lenses.[14–16]

The important figures of merit of the microbeam are the spot size produced on the sample, the intensity gain in the focus, and the absolute flux that can be transferred into the microbeam. Finally, the shape of the spot and its background (that may have low intensity but high integral flux) is important. A controlled and ideally constant thickness of the microbeam at the sample position is favorable, such that thicker samples are scanned with a pencil beam of constant thickness. This is particularly important for scanning tomography application such as fluorescence microtomography.[17]

This article is focused on the microbeam properties of parabolic compound refractive lenses (PCRLs) that are fabricated since 1998. They have been developed at the University of Technology in Aachen, Germany, in collaboration with the European Synchrotron Radiation Facility (ESRF) in Grenoble, France.[18,15,16] Today, several groups throughout the world are producing CRLs.[19–21] They have become a standard tool for microbeam applications and are routinely used at beamlines ID18f and ID22 of the ESRF. In addition, their imaging properties allow to use them as an objective lens in a hard x-ray microscope.[18]

In section 2 the important properties of PCRLs and microbeams are reviewed. The experimental characterization of the microbeams is given in section 3. Two fluorescence microprobe applications are shown in section 4, the fluorescence microtomography of a mycorrhyzal root of the tomato plant (section 4.1) and the imaging of trace element distributions in single cancer cells (section 4.2).

Correspondence: C. G. Schroer. E-mail: schroer@xray-lens.de

X-Ray Micro- and Nano-Focusing: Applications and Techniques II, Ian McNulty, Editor, Proceedings of SPIE Vol. 4499 (2001) © 2001 SPIE · 0277-786X/01/$15.00

2. MICROFOCUSING USING PARABOLIC COMPOUND REFRACTIVE LENSES

2.1. Properties of Parabolic Compound Refractive Lenses

The imaging properties of parabolic compound refractive lenses have been discussed in detail in previous publications.[18,16] However, the thin lens approximation that has been previously used is not always appropriate, in particular for lenses with short focal distance compared to their thickness. Therefore, the focal length of thick compound refractive lenses is considered in more detail below. Other important lens properties, like the effective aperture $D_{\rm eff}$ and the transmission $T_{\rm p}$ are briefly reviewed as they are needed in this article.

The focal distance $f_0 = R/2N\delta$ of a CRL was derived using the thin lens approximation.[9] Here, R is the radius of curvature of each lens surface on the optical axis, N is the number of single lenses stacked behind each other in the CRL, and δ is the index of refraction decrement (complex index of refraction $n = 1 - \delta + i\beta$).

To obtain a short focal distance, a large number N of single lenses needs to be stacked in a PCRL. With a thickness of $\Delta l = 1$mm of a single lens, the overall length of the PCRL ($l = N\Delta l$) can reach a significant fraction of the focal length. In the experimental example considered below, $N = 220$ single lenses should give a nominal focal distance $f_0 = 292$mm at 18.2keV as compared to the length of the lens of $l = 220$mm. Experimentally, a longer focal distance of $f = 328$mm was observed.

To obtain the real focal distance f of the compound system, we use the transfer matrix formalism.[22] Let r be the coordinate perpendicular to the optical axis. A ray is then characterized by its distance r from the optical axis and its slope r' with respect to the optical axis. Given a ray $\begin{pmatrix} r' \\ r \end{pmatrix}$, the effect of an optical element is given by its transfer matrix. Each single lens has a focal distance $f_{\rm s} = R/2\delta$, and the lenses are separated by Δl from each other. Refraction and propagation are each described by a transfer matrix

$$T_{f_{\rm s}} = \begin{bmatrix} 1 & -\frac{1}{f_{\rm s}} \\ 0 & 1 \end{bmatrix} \quad \text{and} \quad T_{\Delta l} = \begin{bmatrix} 1 & 0 \\ \Delta l & 1 \end{bmatrix},$$

respectively. The compound refractive lens is described by the ordered product

$$T_{\rm PCRL} = T_{\Delta l/2}(T_{f_{\rm s}} T_{\Delta l})^{N-1} T_{f_{\rm s}} T_{\Delta l/2}. \tag{1}$$

When the distances between the single lenses are neglected,

$$T_{\rm PCRL} = (T_{f_{\rm s}})^N = \begin{bmatrix} 1 & -N\frac{1}{f_{\rm s}} \\ 0 & 1 \end{bmatrix}$$

and the focal distance $f_0 = \frac{f_{\rm s}}{N} = \frac{R}{2N\delta}$ is recovered. However, when the full expression (1) is evaluated, the focal distance f to leading order of $\Delta l/f_{\rm s}$ is

$$f = f_0 \frac{1}{1 - \frac{1}{6}\frac{l}{f_0}} + O\left(\frac{\Delta l^2}{f_{\rm s}^2}\right) \approx f_0 + \frac{1}{6}l. \tag{2}$$

The principal planes of the compound system coincide at its center. The effect becomes relevant, when $l/6$ is larger than the depth of field of the lens, and the radius of curvature R of the lenses can be determined with sufficient precision.

The effective aperture $D_{\rm eff}$ that describes diffraction and the effects of the lens roughness is always smaller than the geometric aperture $2R_0$, and is given by

$$D_{\rm eff} = 2R_0 \sqrt{\frac{1}{a_{\rm p}}\left[1 - \exp(-a_{\rm p})\right]}, \quad a_{\rm p} = \frac{\mu N R_0^2}{2R} + \frac{N\delta^2 k_1^2 \sigma^2 R_0^2}{R^2}, \tag{3}$$

where k_1 is the wave number of the incident radiation, and σ is the r. m. s. roughness of the lens surfaces. The effective aperture of a lens with $f = 500$mm focal distance is shown in Fig. 1(a) as a function of energy for different lens materials.

The transmission $T_{\rm p}$ through the lens given by

$$T_{\rm p} = \exp(-\mu N d)\frac{1}{2a_p}[1 - \exp(-2a_p)] \tag{4}$$

determines what fraction of the flux incident on the geometric aperture (constant intensity) is transmitted through the lens.

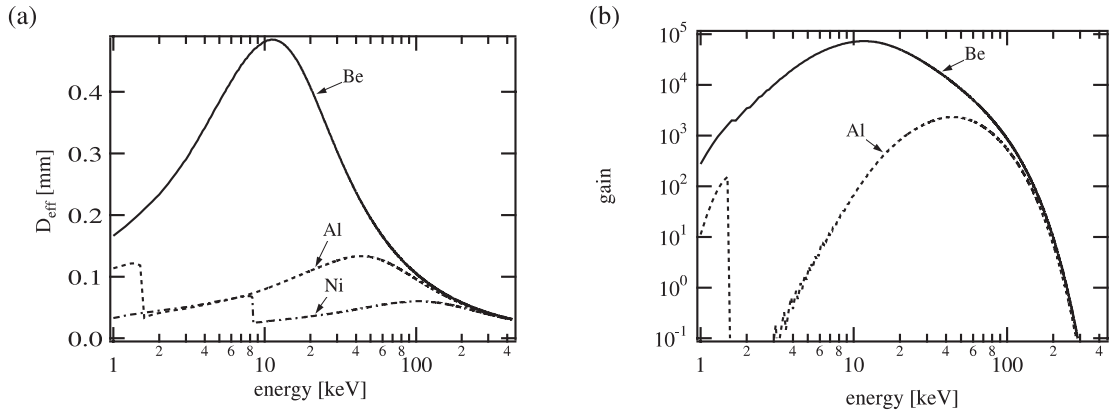

Figure 1. (a) Effective aperture $D_{\rm eff}$ of a parabolic compound refractive lens with focal distance $f = 500$mm for different lens materials (lens thickness $d = 5\mu$m). (b) The gain for a microfocus geometry ($L_1 = 60$m, r. m. s. source size $13 \times 300\mu$m^2 (V $\times$ H)) using the lens in (a).

2.2. Properties of the Monochromatic Microbeam Produced by Parabolic Compound Refractive Lenses

This chapter reviews the properties of monochromatic microbeams obtained by imaging the source onto the sample in a strongly demagnifying geometry. For a source-lens distance L_1 the optimal microbeam is obtained at a distance $L_{2_0} = L_1 f/(L_1 - f)$ behind the lens. For monochromatic radiation, the intensity distribution on the sample was previously calculated,[16] including diffraction at the lens aperture and roughness of the lens surfaces. In an arbitrary plane a distance L_2 behind the lens, the intensity distribution of monochromatic x-rays of energy E is

$$\begin{aligned} I_E(L_2,p,q) &= I_0(E)\, T_p(E)\, A \exp\left\{-(ak_1^2R^2/L_2^2)\right. \\ &\quad \left. \times \left[p^2/(aa_{\rm v} + b^2F^2) + q^2/(aa_{\rm h} + b^2F^2)\right]\right\}, \end{aligned} \tag{5}$$

where (p, q) are the coordinates in the plane L_2 behind the lens, $T_{\rm p}$ is the lens transmission, A normalizes the gaussian to unity, $a = \mu NR + 2Nk_1^2\delta^2\sigma^2$, $b = k_1R^2$, $F = 1/L_1 + 1/L_2 - 1/f$, and $a_{\rm v,h} = a + 2k_1^2R^2\sigma_{\rm v,h}^2/L_1^2$. $\sigma_{\rm v,h}$ are the r.m.s. vertical and horizontal extensions of the source that is well described by the gaussian intensity distribution

$$W(x,y) = \frac{I_0}{2\pi\sigma_{\rm v}\sigma_{\rm h}} \exp\left[-\frac{1}{2}\left(\frac{x^2}{\sigma_{\rm v}^2} + \frac{y^2}{\sigma_{\rm h}^2}\right)\right], \tag{6}$$

where I_0 is the integral intensity. For the undulator source u42 at beamline ID22 of the ESRF the source size is approximately given by $\sigma_{\rm v} = 13\mu$m and $\sigma_{\rm h} = 300\mu$m.[23] However, a sightly larger vertical effective source size is found, that is produced by the monochromator ($\sigma_{\rm v} = 21\mu$m).

The lateral beam size (full width at half maximum (FWHM)) at the optimal focus ($L_2 = L_{2_0}$) can be extracted from eq. (5) and is

$$B_{\rm v,h} = 2\sqrt{2\ln 2}L_{2_0}\sqrt{\sigma_{\rm v,h}^2/L_1^2 + a/(2k_1^2R^2)}. \tag{7}$$

The depth of focus is defined as the distance along the optical axis, in which the lateral beam size is smaller than $\sqrt{2}\, B_{\rm v,h}$ for both the vertical and the horizontal direction. It is

$$d_{\rm long} = 4\frac{B_{\rm v}/(2\sqrt{2\ln 2})\cdot L_2}{D_{\rm eff}}, \tag{8}$$

where we have assumed that $D_{\rm eff}$ is small with respect to the geometrical aperture $2R_0$ of the lens. The gain of intensity obtained in the microbeam is given by

$$g_{\rm p} = T_{\rm p}\frac{4R_0^2}{B_{\rm v}B_{\rm h}}, \tag{9}$$

where $T_{\rm p}$ is the transmission of the lens given by eq. (4). The gain for a typical microbeam geometry is shown in Fig. 1(b) as a function of energy for beryllium and aluminium as lens material.

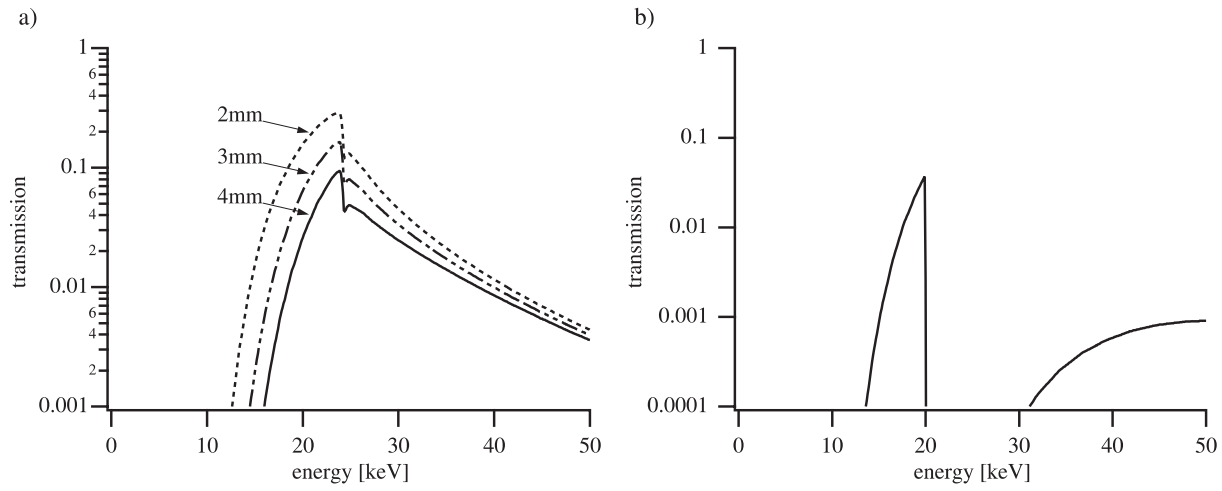

Figure 2. (a) Transmission of a pink beam filter composed of an aluminium absorber (thickness 2mm, 3mm, and 4mm, respectively) and a palladium mirror at an angle of $\theta = 0.15°$. (b) Transmission of a pink beam filter composed of a molybdenum absorber (thickness 250μm) and a palladium mirror at $\theta = 0.15°$.

2.3. Undulator "Pink" Beam: Isolating One Harmonic From the Undulator Spectrum

As a result of interference the spectrum of an undulator source (as measured on the optical axis) is naturally spiked around a certain fundamental energy and its integer multiples (harmonics). The number of magnetic periods N_u in the undulator ($N_u = 38$ for the u42) determines the width of each harmonic that is typically of the order of 1% to 2%.

To produce monochromatic x-rays, the undulator is typically tuned such that the desired energy lies at the maximum of a certain harmonic. A double crystal monochromator then selects a small energy band (typically $\Delta E/E \approx 10^{-4}$) out of the broader spectrum of this harmonic. With a natural band width of the undulator harmonic in the range of $\Delta E/E \approx 1\%$, the monochromatization reduces the flux by about two orders of magnitude. For many experiments, however, the monochromatization to 10^{-4} is not necessary and an increase in flux at the expense of monochromaticity is favorable. Ideally, the undulator spectrum would be reduced to one particular harmonic. This can be approximately achieved by constructing an appropriate band pass at the desired energy using absorbers and mirrors as high and low pass filters, respectively.

Two particular band pass filters are shown in Fig. 2. Both use a Pd total reflexion mirror (reflexion angle $\theta = 0.15°$) that generates a low-pass with cut-off energy at about 24keV. In combination with an aluminium absorber (Fig. 2(a)), a relatively broad (4keV) band pass is produced peaking slightly below 24keV. With the 5th harmonic of the u42 undulator[23] at 23.3keV, the "pink" undulator spectrum shown in Fig. 3(a) is obtained.

Taking advantage of an absorption edge of the filter material, the contamination of the spectrum by neighboring harmonics can be significantly reduced. The band pass filter using a Mo absorber (thickness 250μm) is shown in Fig. 2(b). With the 5th harmonic tuned to 19.7keV, the pink undulator spectrum shown in Fig. 3(b) is obtained. The spectrum shows significantly less contamination from neighboring harmonics. However, this was obtained at the expense of flux that was 3.1 times lower than with the aluminium filter, but still 6.8 times higher than in the monochromatic beam.

Taking advantage of an absorption edge, the energy of the beam is confined to slightly below the edge of the filter material. The aluminium filter, however, can be tuned continuously in a wide range of energies, if the deflection angle θ can be adjusted, and different mirror coatings are available.

2.4. Properties of the "Pink" Microbeam

Refractive x-ray lenses are dispersive optics. To obtain a quantitative description of the polychromatic microbeam, we consider the intensity distribution in an arbitrary plane a distance L_2 behind the lens. For a given energy spectrum

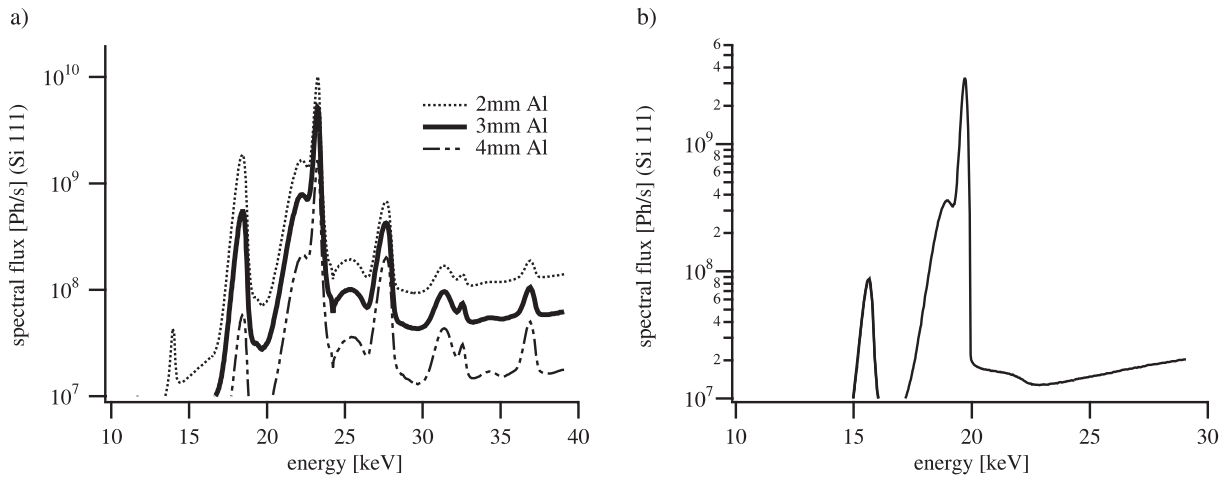

Figure 3. Measured pink beam spectra during single bunch mode (synchrotron current reduced by one order of magnitude). The flux recorded by a single crystal analyzer (Si 111) as a function of energy is shown, (a) using the Al-absorbers in conjunction with the Pd-mirror, (b) using the Mo-absorber with the Pd-mirror.

$\rho(E)$, (5) can be integrated to obtain the polychromatic intensity distribution

$$I(L_2, p, q) = \int \mathrm{d}E\ \rho(E)\ I_E(L_2, p, q). \tag{10}$$

Photons of different energy are differently distributed within this microbeam. As the excitation of fluorescence depends on the energy of the incident radiation, the effective beam shape for the fluorescence microprobe is modified by the energy dependence of the fluorescence cross section. For the fluorescence microprobe, the beam shape is therefore determined by

$$I_{\mathrm{Fl}}(L_2, p, q) \sim \int \mathrm{d}E\ \rho(E)\ \mu_{\mathrm{Fl}}(E)\ I_E(L_2, p, q), \tag{11}$$

where μ_{Fl} is the absorption resulting in the excitation of the fluorescence line of interest. For an arbitrary spectrum, each fluorescence line has its own point response to the microbeam resulting in individual point spread functions (11). In practice, however, for the pink spectra considered, the difference in the intensity distribution between (10) and (11) is small, provided the fluorescence edge is well below the strongly contributing parts of the pink spectrum. For the pink beam spectra considered in section 2.3, this is true for absorption edges below 15keV. In the following, (10) is therefore used to describe the microbeam.

3. EXPERIMENTAL RESULTS

3.1. Characterization of the Monochromatic Microbeam

The microbeam experiments described where carried out at beamline ID22 of the ESRF. The synchrotron radiation was generated by a u42 undulator source.[23] A flat total reflexion mirror coated with Pd was used to remove the higher harmonics. With the total reflexion angle of 0.15° the mirror has a cut-off energy of about 24keV. A Si 111 double crystal monochromator is used to obtain monochromatic radiation.

We have investigated a microbeam produced by a parabolic compound refractive lens with $N = 220$ single lenses at $E = 18.2$keV. With a source to lens distance of $L_1 = 41.7$m, the optimal image distance was found at $L_2 = 331$mm, giving an experimental focal distance of $f = 328$mm. The radius of curvature R of the lens surfaces was measured by profilometry to $R = 209\mu\mathrm{m} \pm 5\mu\mathrm{m}$. In the thin lens approximation, this radius of curvature yields a focal distance of $f_0 = 291\mathrm{mm} \pm 4\mathrm{mm}$ and an image distance $L_2 = 293\mathrm{mm} \pm 4\mathrm{mm}$ that significantly deviates from the measured value of 331mm. Using eq. (2), the focal distance $f = 332\mathrm{mm} \pm 4\mathrm{mm}$ and $L_2 = 335\mathrm{mm} \pm 4\mathrm{mm}$ is in good agreement with the experimental results. Here, the thick lens character of the PCRL adds about 14% to the focal distance.

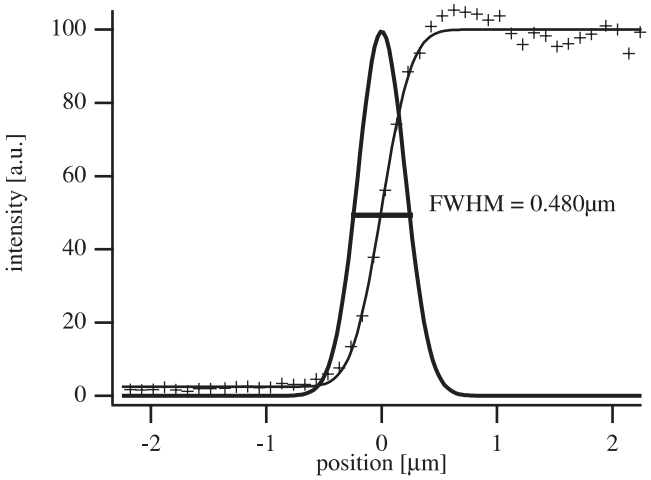

Figure 4. Vertical profile through a microbeam measured by a fluorescence knife edge technique. An error function is fitted to the measured data (crosses). Its derivative gives the vertical profile of the microbeam.

The horizontal and vertical microbeam sizes where measured, using a fluorescence knife edge technique. As knife edge a gold strip (thickness 100nm, width 5mm, length several centimeters) deposited on a silicon wafer (thickness 550μm) was used. The gold Lα radiation ($E = 9.71$keV) was measured by an energy dispersive detector (SiLi) as the gold edge was scanned through the beam. Fig. 4 shows the scan through the microbeam in vertical direction. A vertical beam width of $B_\mathrm{v} = 480$nm was measured. Including diffraction and roughness, a beam size of 450nm is expected.

The horizontal microbeam size is one order of magnitude larger due to the larger source size. It was measured to 5.17μm (FWHM) as compared to the theoretical value of 5.7μm (FWHM). The measured transmission $T_\mathrm{p} = 0.114\%$ yields an average lens thickness of $d = 5\mu$m on the optical axis. The measured gain is 367 as compared to the theoretical value 340 that is slightly smaller due to the discrepancy in the horizontal beam size.

By closing down the primary slits of the beamline at a distance of 28.4m from the source, the effective horizontal source size can be reduced at the expense of flux. For a gap of the slit of 0.1mm, for example, a horizontal source size of 2.2μm can be obtained. To minimize the losses in flux, the slits should be positioned right after the undulator source.

The background of the microbeam contributes to the signal obtained in microprobe applications. In principle, a deconvolution with the point spread function is necessary to remove the contribution of the background. Although the intensity of the background radiation is generally small, it may contribute significantly to the signal, since the area over which it is integrated is several orders of magnitude larger than the lateral area of the microbeam. The background is therefore an important characteristic of the microbeam.

As the dimensions of the knife edge are large compared to the beam size, the flux $\Phi(p_0)$ measured by the knife edge technique may be considered as the integral intensity

$$\Phi(p_0) = \int_{-\infty}^{\infty} \mathrm{d}q \int_{-\infty}^{p_0} \mathrm{d}p \; I(L_2, p, q), \tag{12}$$

over the half-plane below $p = p_0$. This allows to measure the integral flux outside the microbeam and to compare it to that in the beam spot.* The knife edge scan shown in Fig. 4 can be evaluated in view of the background. The integral flux that falls outside a vertical interval $[-2\mu\mathrm{m}, 2\mu\mathrm{m}]$ around the spot is about 3.4%, the flux falling outside the interval $[-1\mu\mathrm{m}, 1\mu\mathrm{m}]$ is 4.6% and that falling outside $[-0.5\mu\mathrm{m}, 0.5\mu\mathrm{m}]$ is 10.4%. Therefore, the monochromatic microbeam produced by the PCRL has a low background and is well suited for clean microprobe experiments. No additional pinholes are needed in front of the sample.

*The knife edge technique allows to measure the horizontal and vertical beam properties independently. An alternative method using fluorescence pads[24] was not available at the time of the experiments and does not allow to discriminate between horizontal and vertical beam properties.

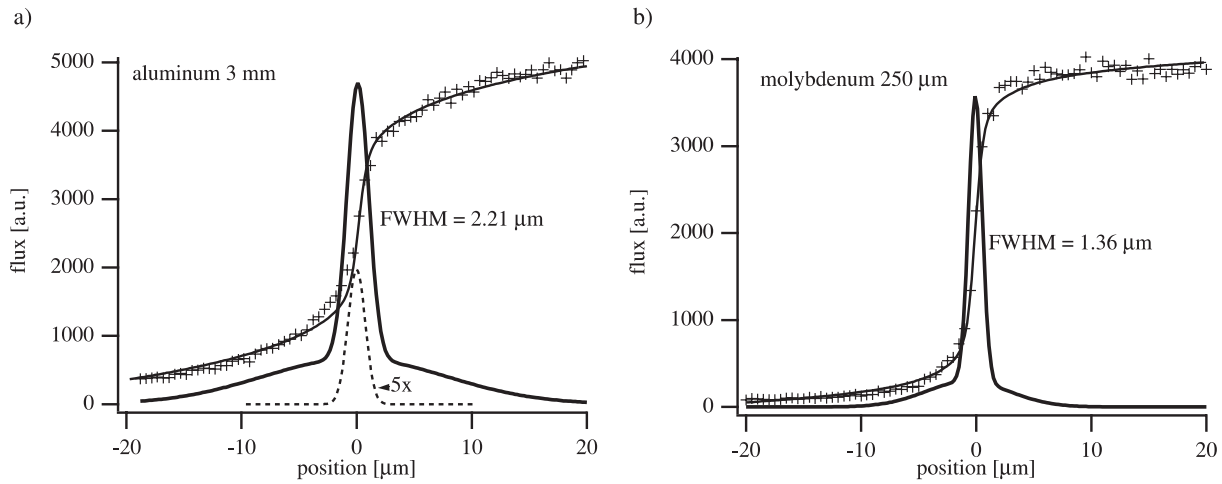

Figure 5. Vertical intensity profile of the microbeam measured in fluorescence by a gold knife edge technique for (a) the Al (3mm) and (b) the molybdenum pink beam filter. The thin solid line depicts the calculated profile as given by (10) from the spectra in Fig. 3. The pink microbeam profile is shown as the solid line. The dashed line in (a) shows the monochromatic microbeam profile (scaled by a factor 5).

3.2. Characterization of Pink Microbeams

The lateral beam size, the flux, and the background for the two types of pink beam filters introduced in section 2.3 are compared to those obtained using monochromatic x-rays. A compound refractive lens was placed a distance $L_1 = 40.7$m away from the undulator source u42 of beamline ID22 at the ESRF. A Pd coated total reflection mirror ($\theta = 0.15°$) was introduced into the beam 33.7m behind the source during the whole experiment. To obtain a monochromatic beam, the fixed exit Si 111 double crystal monochromator was moved into the beam at 36m behind the source whenever it was needed.

Since the vertical beam size is much smaller than the horizontal one, it is more sensitive to imaging errors and aberrations. Therefore, it is considered in more detail below. The horizontal beam size is discussed in the fluorescence microtomography application in section 4.1.

3.3. Example: Pink Beam with Al Filter

An aluminium PCRL with $N = 80$ was used to produce a pink microbeam using the Al(3mm)/Pd(0.15°) filter combination. The spectrum incident on the lens is shown in Fig. 3(a). For the maximum intensity at 23.3keV the microfocus is formed at the sample position $L_2 = 1253$mm behind the lens, where the gold knife edge was positioned.

The measured fluorescence intensity as a function of vertical position of the knife edge is shown in Fig. 5(a) as crosses. This measurement can be fitted very accurately by two superimposed error functions. Their derivative yields the vertical intensity distribution shown in Fig. 5(a) as the thick solid line. The vertical FWHM size of the microbeam is measured to 2.21μm to be compared to the ideal monochromatic spot of 1.0μm. Note that there is a significant background that extends several widths of the central peak away from the center of the distribution. Using (11) and the spectrum in Fig. 3(a), the knife edge measurement (calculated integral flux) is well reproduced from the theory of imaging with CRLs and is depicted by the thin solid line in Fig. 5(a).

The background can be extracted from Fig. 5(a). 14% of the radiation fall outside the interval $[-20\mu\text{m}, 20\mu\text{m}]$, 25%(2.3%) lie outside $[-10\mu\text{m}, 10\mu\text{m}]$, 40%(3.6%) outside $[-5\mu\text{m}, 5\mu\text{m}]$, and 52%(8.2%) outside the interval $[-2.5\mu\text{m}, 2.5\mu\text{m}]$ as compared to the monochromatic (23.3keV) background radiation shown in brackets. The FWHM extension of the monochromatic beam was measured to 1.7μm. The monochromatic spot scaled by a factor 5 is shown as the dashed line in Fig. 5(a). Integrally, the pink beam is 28 times more intensive than the monochromatic beam. However, a large fraction of the flux of the pink beam contributes to the background, and the peak intensity is about 12 times higher than that of the monochromatic beam.

3.4. Example: Pink Beam with Mo Filter

The main energy in the pink beam spectrum produced by the molybdenum/palladium filter combination (Fig. 3(b)) lies at 19.7keV. To obtain a comparable setup to the one in section 3.3, $N = 59$ single lenses were used to compose the PCRL. At a distance $L_2 = 1183$mm the optimal microbeam was measured by the knife edge technique. The crosses in Fig. 5(b) show the measured data. The thin solid line depicts the calculated integral flux on the knife edge using the spectrum in Fig. 3(b) and eq. (10). The intensity distribution in the spot was obtained by fitting the sum of two error functions to the knife edge measurement and taking its derivative. The thick solid line in Fig. 3(b) shows this distribution. The vertical FWHM size of the microbeam is 1.36μm.

The background was extracted from Fig. 5(b). 2.6% of the radiation fall outside the interval $[-20\mu\text{m}, 20\mu\text{m}]$, 8.5%(2.0%) lie outside $[-10\mu\text{m}, 10\mu\text{m}]$, 15.2%(5.1%) outside $[-5\mu\text{m}, 5\mu\text{m}]$, and 23.3%(13%) outside the interval $[-2.5\mu\text{m}, 2.5\mu\text{m}]$ as compared to the monochromatic (19.8keV) background radiation shown in brackets. Integrally, the intensity in the pink microbeam is 5.6 times higher than in the monochromatic beam, and the background contribution is small, in particular because the high energies that are easily transmitted through the lens are strongly suppressed by the Mo K-edge. Therefore, this microbeam is very well suited for high resolution microanalytical applications. In section 4.1 we give an example of a microanalytical experiment using a Mo/Pd filtered pink beam.

3.5. Example: Pinhole Pink Beam Filter

An alternative filter can be implemented using a pinhole in front of the sample. Besides the pinhole, the Pd-mirror is used to suppress the radiation above 24keV. For the experiment described in section 4.2, a 10μm pinhole was used to implement a microbeam at 14keV. A compound refractive lens ($N = 50$) was used to image the undulator source at beamline ID22 (5th harmonic at 14keV) to the sample position $L_2 = 713$mm behind the lens. The FWHM of this filter is 2.6keV.

4. APPLICATIONS

4.1. Fluorescence Microtomography of a Mycorrhizal Root of the Tomato Plant

During a fluorescence microtomography experiment at the ESRF, a Mo/Pd filtered pink microbeam was produced using a CRL with $N = 220$ single lenses. The lens was positioned $L_1 = 41.7$m away from the source and the microbeam was formed $L_2 = 396$mm behind the lens. The vertical spot size of the pink beam was measured to 840nm (FWHM) as compared to 480nm for the monochromatic beam.

Using the microbeam a fluorescence microtomogram of the mycorrhizal root of the tomato plant was recorded. Details of this method and about this experiment can be found in.[25,26,17] The sample was scanned horizontally through the beam in 105 steps of 1μm to obtain one tomographic projection. The fluorescence signal emanating from the plant was recorded by an energy dispersive detector (SiLi) during 2s at each step, as well as the primary and transmitted intensity by two PIN-diodes. After a projection, the sample was rotated by an integer fraction of 360° and the next projection is recorded. In all, 132 projections were recorded to obtain the full tomographic data.

The resolution of the experiment was limited by the horizontal spot size, that was controlled by closing the primary horizontal slits a distance 28.4m behind the source. With the slits closed to 100μm, a horizontal spot size of 1.92μm FWHM was obtained. A background of 12% outside the interval $[-2.5\mu\text{m}, 2.5\mu\text{m}]$ and 8% outside $[-5\mu\text{m}, 5\mu\text{m}]$ was measured. The flux in the pink microbeam was measured to 2.3×10^9 ph/s, which is 9.2 times higher than for the monochromatic radiation using a Si 111 double crystal monochromator.

The tomographic reconstruction was done by an iterative method taking self-absorption effects of the sample into account. Details on the tomographic model as well as the reconstruction technique can be found in.[26,27] Fig. 6 shows the reconstructed distributions of potassium (K), iron (Fe), zinc (Zn), and the attenuation coefficient μ_0 at $E_0 = 19.7$keV on a slice through the root. To obtain a sufficiently high number of fluorescence counts for the channels of interest, two second acquisition time per point was required. The total acquisition time in this experiment was 7 hours and 42 minutes. Therefore, the experiment would not have been feasible using monochromatic x-rays, as the acquisition times would have been almost one order of magnitude longer.

Fluorescence microtomography allows the element mapping inside delicate biological samples with high sensitivity. In this case, it was used to localize pollutants inside the root of a tomato plant.

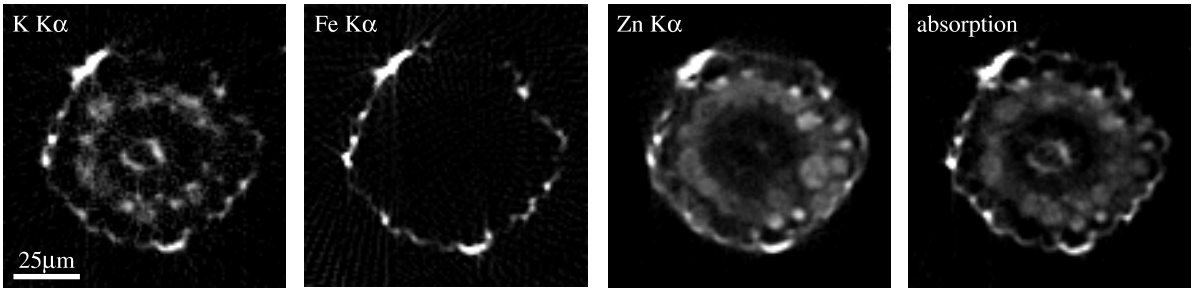

Figure 6. Reconstructed distribution of potassium (K), iron (Fe), zinc (Zn), and the attenuation μ_0 of the mycorrhizal root of a tomato plant. The resolution is $< 2\mu$m.

4.2. Synchrotron Induced X-ray Fluorescence on Cancer Cells

Spatial distribution and concentration of trace elements in tissues are of importance as they are involved in many biological functions of living organisms like metabolism and nutrition. Some trace elements have been shown to play a role in pathological conditions (e. g., cancer). The importance of the microanalysis of individual cells has been reviewed by Llabador and Moretto,[28] who emphasized the future importance of microprobe techniques for some problems in cell physiology, cell pharmacology and for toxicology from heavy elements.

Further insight into biological processes and cellular analysis requires mainly high spatial resolution techniques for intracellular analysis, quantitative data, non-destructive analysis and chemical information. These requirements can be fulfilled by recent improvements that have been realized in synchrotron x-ray sources (third generation) and in x-ray focusing optics (e. g., parabolic CRLs). Highly collimated quasi-monochromatic x-ray beams with tunable energy and highly focused beams with (sub-)micrometer diameter can be used for trace element analysis (x-ray fluorescence), chemical speciation (XANES) with minimum radiation damage to the sample, short-time analysis and low detection limit (< ppm).

The experiment reported here has been described in detail elsewhere.[29] Elemental imaging of cells treated with 5μM (pharmacological dose) of the anticancer drug 4-iodo-4-deoxydoxorubicin (IDX) used here can not be performed by proton induced x-ray emission (PIXE) due to excessive time of analysis and sample damaging.

This work was made in collaboration with R. Ortega from the Laboratoire de Chimie Nucléaire Analytique et Bioenvironnementale in Bordeaux.[30] With the 5th undulator harmonic at 14keV, the pink beam filter described in section 3.5 was implemented using a compound refractive lens ($N = 50$) and a 10μm pinhole at a distance slightly smaller than the lens-sample distance $L_2 = 713$mm. This way, a spot size of $1 \times 10\mu\text{m}^2$ (vertical $\times$ horizontal) and a flux of about 5×10^{10} ph/s/μm^2 was obtained. Freeze-dried cells were prepared as previously described.[31] The experiment confirms that under our conditions, high energy, high intensity x-rays are well suited for microanalysis of sensitive biological specimen. Results show high accuracy in trace elements measurements for cells treated with pharmacological doses of an anticancer drug (Fig. 7). This result could not have been obtained by PIXE, as the concentrations of the elements of interest are too low for this method. The co-localization of iron and iodine within the cell nucleus previously observed in PIXE for higher doses of the drug is still observed in our study. Comparable results have been obtained using PIXE for a higher dose of the drug.[31] Maximum concentrations are around $1.4\mu\text{g/cm}^2$ for potassium, $0.025\mu\text{g/cm}^2$ for iron except in an artifact of preparation observed as a spot slightly to the left of the center in the map (Fig. 7) were the concentration goes up to $0.34\mu\text{g/cm}^2$, and for iodine $0.23\mu\text{g/cm}^2$.

In conclusion synchrotron x-ray fluorescence (SXRF) analysis on single-cells is at its starting point and is expected to become a powerful non-destructive method, complementary to cellular experiments carried out in particle induced x-ray emission.

5. CONCLUSION AND OUTLOOK

The imaging properties of parabolic lenses are well understood and the lens quality is such that the experimental results agree well with theoretical considerations for ideal parabolic lenses. Aluminium PCRLs are routinely used for microbeam production at two ESRF beamlines. They are compatible with the high heat load of undulator sources

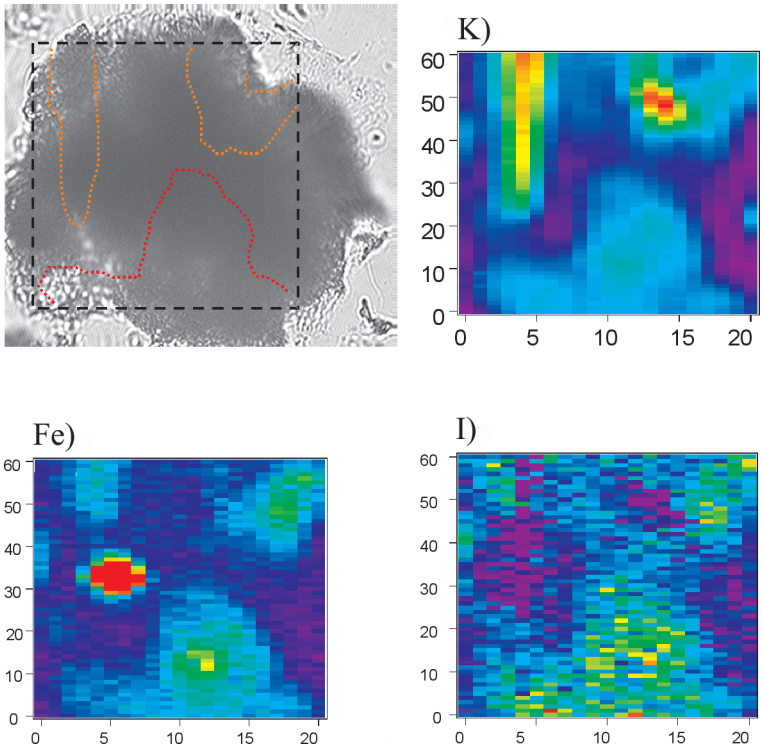

Figure 7. Two dimensional elemental imaging of several cancer cells that were treated with 5μM of iodo-deoxydoxorubicin and subsequently freeze-dried. On the upper left the optical microscope image of a group of cells is shown that was mapped exciting the fluorescence with a 14keV polychromatic pink beam, using a step size of $1 \times 3\mu$m (V $\times$ H), and 2.5s acquisition time/step. Around 2 hours were required for the acquisition. The distribution within the cells of potassium (K) and iron (Fe) Kα and Iodine (I) Lβ radiation are represented in the 2-D maps. The dashed line serves as a guide to the eye and depicts boundaries in the map on the optical microscope image. The high concentration of iron localized as a spot slightly to the left of the center of the image is an artifact produced in cell preparation.

and can be used with "pink" undulator radiation, allowing to increase the flux in the microbeam by about one order of magnitude. Using more transparent lens materials, such as beryllium, will increase the transmission of the lens by about two orders of magnitude, significantly improving the flux and gain of the microprobe.

ACKNOWLEDGMENTS

The microfocusing experiments where carried out at the ESRF during ID22 inhouse research and the user experiments MI-318 and LS-1739. We would like to thank H. Schlösser from the II. Physikalisches Institut of the Aachen University of Technology for his strong commitment to fabricating PCRLs of high quality. We also thank J. M. Rigal for his excellent support during the experiments.

REFERENCES

1. P. Kirkpatrick and A. Baez, "Formation of optical images by x-rays," *J. Opt. Soc. Am.* **38**(9), pp. 766–774, 1948.
2. Y. Suzuki and F. Uchida, "Hard x-ray microprobe with total-reflection mirrors," *Rev. Sci. Instrum.* **63**, pp. 578–581, January 1992.
3. J. Underwood, T. Barbee Jr., and C. Frieber, "X-ray microscope with multilayer mirror," *Appl. Opt.* **25**, pp. 1730–1732, June 1986.
4. J. Underwood, A. Thompson, Y. Wu, and R. Giauque, "X-ray microprobe using multilayer mirrors," *Nucl. Instrum. Methods A* **266**, pp. 296–302, 1988.
5. D. Bilderback, S. A. Hoffman, and D. Thiel, "Nanometer spatial resolution achieved in hard x-ray imaging and Laue diffraction experiments," *Science* **263**, pp. 201–203, 1994.
6. S. A. Hoffman, D. J. Thiel, and D. H. Bilderback *Nucl. Instrum. Methods A* **347**, p. 384, 1994.
7. B. Lai, W. Yun, D. Legnini, Y. Xiao, J. Chrzas, P. Viccaro, V. White, S. Bajikar, D. Denton, F. Cerrina, E. Fabrizio, M. Gentili, L. Grella, and M. Baciocchi, "Hard x-ray phase zone plate fabricated by lithographic techniques," *Appl. Phys. Lett.* **61**(16), pp. 1877–1879, 1992.
8. P. Chevallier, P. Dhez, F. Legrand, M. Idir, G. Soullie, A. Mirone, A. Erko, A. Snigirev, I. Snigereva, A. Suvorov, A. Freund, P. Engström, J. A. Nielsen, and A. Grübel, "First test of the scanning x-ray microprobe with Bragg-Fresnel multilayer lens at ESRF beam line," *Nucl. Instrum. Methods A* **354**, pp. 584–587, 1995.
9. A. Snigirev, V. Kohn, I. Snigireva, and B. Lengeler, "A compound refractive lens for focusing high energy x-rays," *Nature (London)* **384**, p. 49, 1996.
10. B. Cederström, R. N. Cahn, M. Danielsson, M. Lundqvist, and D. R. Nygren, "Focusing hard X-rays with old LP's," *Nature* **404**, p. 951, 2000.
11. B. Cederström, M. Danielsson, and M. Lundqvist, "Refractive beryllium X-ray lens with variable focal length," in *Advances in X-ray Optics*, A. K. Freund, T. Ishikawa, A. M. Khounsary, D. C. Mancini, A. G. Michette, and S. Oestreich, eds., vol. 4145 of *Proceedings of the SPIE*, 2001.
12. V. Aristov, M. Grigoriev, S. Kuznetsov, L. Shabelnikov, V. Yunkin, T. Weitkamp, C. Rau, I. Snigireva, and A. Snigirev, "X-ray refractive planar lens with minimized absorption," *Appl. Phys. Lett.* **77**(24), pp. 4058–4060, 2000.
13. Y. Zhang, T. Katoh, Y. Kagoshima, J. Matui, and Y. Tsusaka, "Focusing hard x-ray with a single lens," *Jpn. J. Appl. Phys.* **40**, pp. L75–L77, 2001.
14. P. Elleaume, "Optimization of compound refractive lenses for x-rays," *Nucl. Instrum. Methods A* **412**, pp. 483–506, 1998.
15. B. Lengeler, C. G. Schroer, M. Richwin, J. Tümmler, M. Drakopoulos, A. Snigirev, and I. Snigireva, "A microscope for hard x-rays based on parabolic compound refractive lenses," *Appl. Phys. Lett.* **74**(26), pp. 3924–3926, 1999.
16. B. Lengeler, C. Schroer, J. Tümmler, B. Benner, M. Richwin, A. Snigirev, I. Snigireva, and M. Drakopoulos, "Imaging by parabolic refractive lenses in the hard x-ray range," *J. Synchrotron Rad.* **6**, pp. 1153–1167, 1999.
17. C. G. Schroer, B. Benner, T. F. Günzler, M. Kuhlmann, B. Lengeler, W. H. Schröder, A. J. Kuhn, A. S. Simionovici, A. Snigirev, and I. Snigireva, "High resolution element mapping inside biological samples using fluorescence microtomography," in *Developments in X-Ray Tomography III*, U. Bonse, ed., vol. 4503 of *Proceedings of the SPIE*, 2001. To be published.

18. B. Lengeler, J. Tümmler, A. Snigirev, I. Snigireva, and C. Raven, "Transmission and gain of singly and doubly focusing refractive x-ray lenses," *J. Appl. Phys.* **84**(11), pp. 5855–5861, 1998.
19. Y. Kohmura, M. Awaji, Y. Suzuki, T. Ishikawa, Y. I. Dudchik, N. N. Kolchewsky, and F. F. Komarow, "X-ray focusing test and x-ray imaging test by a microcapillary x-ray lens at an undulator beamline," *Rev. Sci. Instrum.* **70**(11), pp. 4161–4167, 1999.
20. Y. I. Dudchik, N. N. Kolchevsky, F. F. Komarov, Y. Kohmura, M. Awaji, and Y. S. andn T. Ishikava, "Glass capillary x-ray lens: fabrication technique and ray tracing calculations," *Nucl. Instrum. Methods A* **454**, pp. 512–519, 2000.
21. M. A. Piestrup, J. T. Cremer, H. R. Beguiristain, C. K. Gary, and R. H. Pantell, "Two-dimensional x-ray focusing from compound lenses made of plastic," *Rev. Sci. Instrum.* **71**(12), pp. 4375–4379, 2000.
22. E. Hecht, *Optics*, Addison-Wesley, Reading, 1987.
23. ID22 beamline handbook, www.esrf.fr/exp_facilities/ID22/handbook.html.
24. A. C. Thompson, J. H. Underwood, E. H. Anderson, and S. A. McHugo, "Characterization of the quality of focused x-ray beams using microfabricated patterns," in *X-Ray Mirror, Crystals, and Multilayers*, A. M. Khounsary, ed., vol. 4145 of *Proceedings of the SPIE*, 2000.
25. A. Simionovici, M. Chukalina, M. Drakopoulos, I. Snigireva, A. Snigirev, C. Schroer, B. Lengeler, K. Janssens, and F. Adams, "X-ray fluorescence microtomography: experiment and reconstruction," in *Developments in X-ray Tomography II*, U. Bonse, ed., vol. 3772 of *Proceedings of the SPIE*, pp. 328–337, SPIE, (Bellingham), 1999.
26. C. G. Schroer, J. Tümmler, T. F. Günzler, B. Lengeler, W. H. Schröder, A. J. Kuhn, A. S. Simionovici, A. Snigirev, and I. Snigireva, "Fluorescence microtomography: External mapping of elements inside biological samples," in *Penetrating Radiation Systems and Applications II*, F. P. Doty, H. B. Barber, H. Roehrig, and E. J. Morton, eds., vol. 4142 of *Proceedings of the SPIE*, pp. 287–296, SPIE, (Bellingham), 2000.
27. C. G. Schroer, "Reconstructing x-ray fluorescence microtomograms," *Appl. Phys. Lett.* , 2001. To be published.
28. Y. Llabador and P. Moretto, *Nuclear microprobe in the Life Science*, World Scientific, Singapore, 1997.
29. S. Bohic, A. Simionovici, A. Snigirev, R. Ortega, G. Devès, D. Heymann, and C. G. Schroer, "Synchrotron hard x-ray microprobe: Fluorescence imaging of single cells," *Appl. Phys. Lett.* **78**, pp. 3544–3546, 2001.
30. S. Bohic, A. Simionovici, R. Ortega, D. Heymann, and A. Snigirev, "Synchrotron induced x-ray microfluorescence on single-cells," in *7th International Conference on Nuclear Microprobe Technology and Applications (ICNMTA-2000)*, (Bordeaux, France), 10-15 Sept. 2000.
31. R. Ortega, P. Moretto, A. Fajac, J. Benard, Y. Llabador, and M. Simonoff *Nucl. Inst. and Methods Phys. Res.* **B 130**, p. 426, 1997.